



Monolithically Integrated Coaxial Resonator-Based Filtennas Using SLA Three-Dimensional Printing

Kunchen Zhao , *Graduate Student Member, IEEE*, and Dimitra Psychogiou , *Senior Member, IEEE*

Abstract—This letter reports on a new class of highly-miniaturized coaxial-resonator-based filtennas alongside a monolithic integration concept using digital additive manufacturing. The filtenna approach is based on the co-design of a coaxial cavity resonator and an annular slot antenna that collectively perform as a radiating resonating node within a coupled-resonator-based bandpass filter. Beam direction can be controlled by altering the position of the radiating slot. A stereolithography apparatus (SLA) monolithic integration concept is proposed for size compactness and reduced weight. For proof-of-concept validation purposes, first-, second-, and third-order filtennas were analyzed through electromagnetic simulations. Experimental validation was performed through the manufacturing and testing of a second-order top-slot filtenna, a second-order and a third-order side-slot filtenna with the following characteristics: center frequency: 4.75 GHz, 4.8 GHz and 4.6 GHz, fractional bandwidth: 7.4%, 8.3%, and 7.6% and realized gain: 5.5 dBi, 2.6 dBi, and 2.6 dBi.

Index Terms—Additive manufacturing, cavity resonator, cavity-backed antenna, coaxial resonator, filtenna, three-dimensional (3-D) printing.

I. INTRODUCTION

THE rapid growth of wireless technologies is increasingly creating the need for small form factor and low weight RF transceivers. RF co-design has been identified as one of the most effective size reduction techniques due to reducing the number of components in RF front end. Typical examples of this trend include co-designed bandpass filters (BPFs) and power dividers [1], BPFs and RF circulators [2], and BPFs and antennas [3], [4], [5], the so-called filtenna concept.

The majority of the filtennas to date are based on microstrip or substrate integrated waveguide (SIW) integration approaches [3], [4], [5], which result in low antenna efficiency. For example, the SIW-based filtenna in [5] exhibits an efficiency of 59% at 3.7 GHz. Metallic waveguide-based filtennas exhibit lower loss as shown in [6], for a cavity-backed slot antenna with an efficiency of 88%. However, these types of approaches exhibit large volume ($>0.25 \lambda_0^3$). Furthermore, they consist of multiple CNC-machined parts that need to be assembled with screws which further increase the complexity, size, and overall weight.

Manuscript received 15 August 2022; accepted 7 September 2022. Date of publication 15 September 2022; date of current version 5 January 2023. This work was supported in part by Science Foundation Ireland (SFI) under Grant 20/RP/8334. (Corresponding author: Kunchen Zhao.)

Kunchen Zhao is with the Department of Electrical, Computer, and Energy Engineering, University of Colorado, Boulder, CO 80309 USA (e-mail: kunchen.zhao@colorado.edu).

Dimitra Psychogiou is with the Department of Electrical and Electronic Engineering, University College Cork, T12 K8AF Cork, Ireland, and also with the Tyndall National Institute, T12 R5CP Cork, Ireland (e-mail: dpsychogiou@ucc.ie).

Digital Object Identifier 10.1109/LAWP.2022.3206757

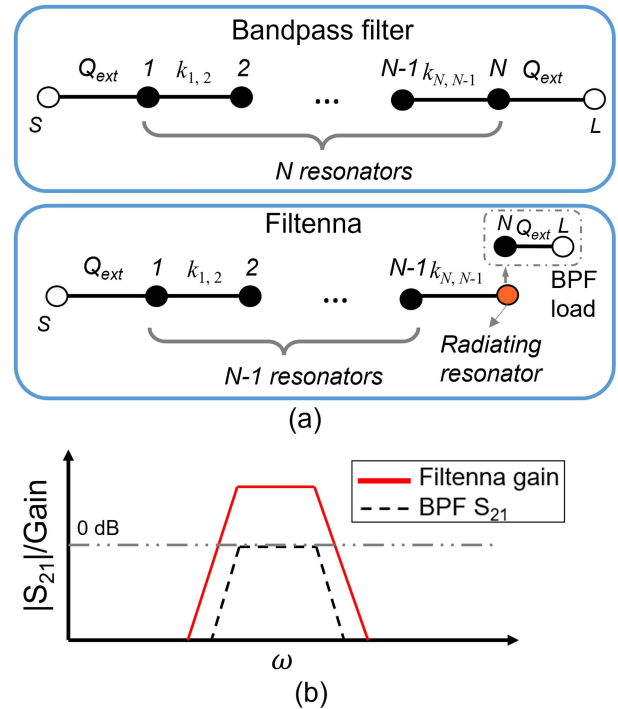


Fig. 1. (a) Conceptual coupling routing diagram of an N th-order BPF and an N th-order filtenna. Black circles: resonating nodes, white circles: source and load, orange circle: radiating resonant node, black lines: couplings. (b) Conceptual power transmission response $|S_{21}|$ of the BPF and gain of the filtenna in (a).

In the recent years, digital additive manufacturing (DAM) has become a low-cost alternative for prototyping antenna elements. Metal-based AM process such as direct metal laser sintering (DMLS) [7] or selective laser melting (SLM) [8], [9] offers high mechanical robustness, but with relatively higher cost and low surface roughness. Ceramic-based or plastic/resin-based AM process [10], e.g., fused deposition modeling (FDM) [11], [12], [13], [14], [15], [16], [17], PolyJet [18], and stereolithography apparatus (SLA) [19], [20], [21] exhibit significantly lower cost and weight. However, due to the need for internal metallization they can only be implemented as split-blocks. On the other hand, monolithic SLA integration concepts have only been demonstrated for open-ended waveguide structures [20], [21]. Considering the aforementioned limitations, this letter reports on the first time a monolithic SLA based-integration concept for a new class of coaxial-resonator-based filtenna. Size compactness is achieved through the: 1) RF co-design of two RF components, 2) use of miniaturized capacitively loaded coaxial resonators, and 3) monolithic integration enabled by SLA manufacturing.

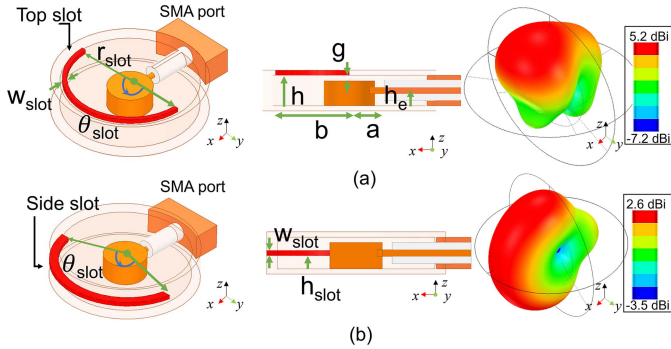


Fig. 2. Three-dimensional simulation model and gain pattern of the radiating resonator at 4.8 GHz. (a) Radiating slot positioned on the top wall. (b) Radiating slot positioned on the side wall. In these examples: $a = 5$, $b = 15$, $h = 6$, $g = 0.75$, $h_e = 3$, $w_{\text{slot}} = 1$ and all units are in mm. Red areas represent the air-filled slot.

II. THEORETICAL FOUNDATIONS

The conceptual coupling routing diagram (CRD) and power transmission coefficient $|S_{21}|$ of an N th-order BPF, and the CRD and gain of an N th-order filtenna are depicted in Fig. 1. The filtenna is created by replacing the last resonator and the load in the CRD of a conventional coupled-resonator-based BPF by a radiating resonating node. To achieve the same power reflection response, the radiating resonator must present the same impedance loading as the last resonator (N) and its preceding impedance inverter (Q_{ext}) in the conventional BPF. In what follows, the designs of the radiating resonator and the coaxial-resonator-based filtenna are provided.

A. Radiating Resonator Concept

The coaxial cavity radiating resonator concept is based on two annular slot antenna configurations, namely the top-slot and the side-slot in Fig. 2(a) and (b)—and a capacitively loaded coaxial cavity resonator. The frequency of the resonator is determined by the capacitive gap g between the upper wall of the cavity and the apex of the post, the radius ratio of the cavity b and the post a and the resonator height h [22]. The RF signal is coupled into the cavity by connecting the SMA connector to the post. The radiation pattern direction can be altered by placing the slot in different locations. When the slot is placed on the upper wall [see Fig. 2(a)], the main lobe is directed in the z -direction with a maximum gain of 5.2 dBi. In yet another configuration, the slot can be placed on the front side wall [see Fig. 2(b)] and in this case the antenna pattern is directed towards the x -axis with a gain of 2.6 dBi. As shown, the top-slot design exhibits higher gain due to the presence of a larger ground plane around the radiating slot and the bottom wall of the resonator that acts as an additional ground plane. Depending on the desired direction of radiation/gain, either of these configurations can be used.

As an initial design, the length of the slot is chosen around $\lambda_0/2$. However, when added on the resonator its resonance frequency will change due to the slot loading. For the top-slot configuration, the resonant frequency is altered by changing the radius r_{slot} and the angle θ_{slot} of the, as shown in Fig. 3(a) and (b). In particular, the operating frequency decreases when the r_{slot} or θ_{slot} increases. Alternatively, the frequency can be tuned by changing g of the coaxial-cavity resonator [see Fig. 4(a)]. For the side-slot configuration, the frequency is dependent on the θ_{slot} , and the slot height does not affect the frequency, as shown in Fig. 3(e) and (f). Fig. 3(c) and (g) illustrates the electric

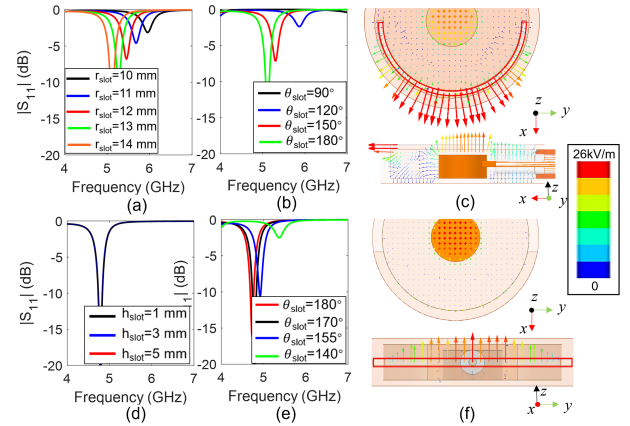


Fig. 3. $|S_{11}|$ of the radiating resonator in Fig. 2(a) for different geometrical parameters. (a) r_{slot} . (b) θ_{slot} . (c) E-field distribution at the upper wall and inside the radiating resonator in Fig. 2(a) at 4.8 GHz. (d) $|S_{11}|$ of the radiating resonator in Fig. 2(b) for different h_{slot} . (e) θ_{slot} . (f) E-field distribution at the side wall of the radiating resonator in Fig. 2(b) at 4.8 GHz.

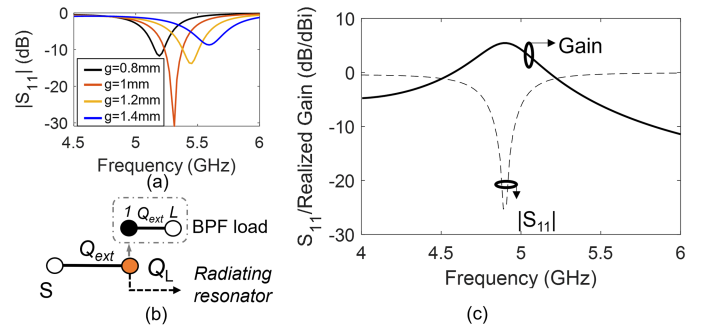


Fig. 4. (a) $|S_{11}|$ of the top-slot radiating resonator in Fig. 2(a) for different gap size g . (b) CRD of a first-order coaxial-resonator-based filtenna. (c) Maximum realized gain as a function of frequency and $|S_{11}|$ for the top-slot first-order coaxial-resonator-based filtenna in Fig. 2(a).

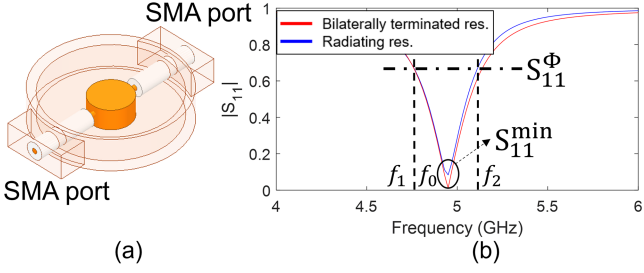
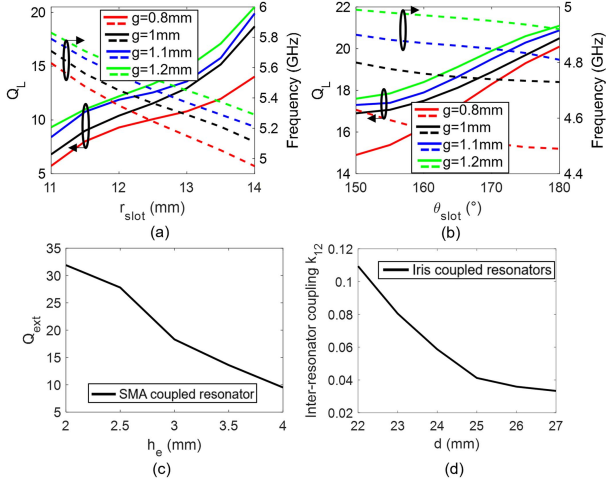
(E)-field distribution on the surface of the upper and side wall of the radiating resonator at 4.8 GHz. As noticed, the quasi-TEM mode of the coaxial cavity is excited [22], where the E-field is strong around the post area due to the capacitive loading of the resonator, and the strongest E-field is observed around the slot. Furthermore, the E-field is transversal to the slot width, indicating that the antennas are linearly polarized.

B. Filtenna Design: First Order

The CRD of a first-order filtenna is shown in Fig. 4(b). It is comprised of a radiating resonator with a loaded quality factor Q_L that is connected to the source via an external coupling element Q_{ext} whose values can be calculated using

$$Q_{\text{ext}} = \frac{1}{m_{01}^2 \cdot \text{FBW}}, \quad Q_L = \left(\frac{1}{Q_{\text{ext}}} + \frac{1}{Q_U} \right)^{-1} \quad (1)$$

where m_{01} is the normalized coupling coefficient and Q_U is the unloaded quality factor of the resonator. For impedance matching, the Q_L of the radiating resonator must be equal to the Q_L of the resonator in the conventional BPF. Thus, the first-order filtennas [see Fig. 2(a) and (b)] and the bilaterally coupled resonator [see Fig. 5(a)] are used to extract Q_L


 Fig. 5. Bilaterally terminated coaxial cavity resonator. (a) Geometry. (b) $|S_{11}|$.

 Fig. 6. (a) Q_L and f_{cen} as a function of r_{slot} for the top slot [see Fig. 2(a)] configuration when $\theta_{slot} = 180^\circ$. (b) Q_L and f_{cen} as a function of θ_{slot} for the side-slot [see Fig. 2(b)]. (c) Q_{ext} as a function of h_e . (d) k_{12} as a function of d . Q_{ext} and k_{12} are calculated at 4.8 GHz.

using [5]

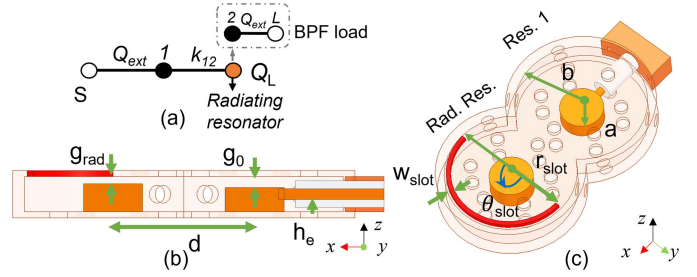
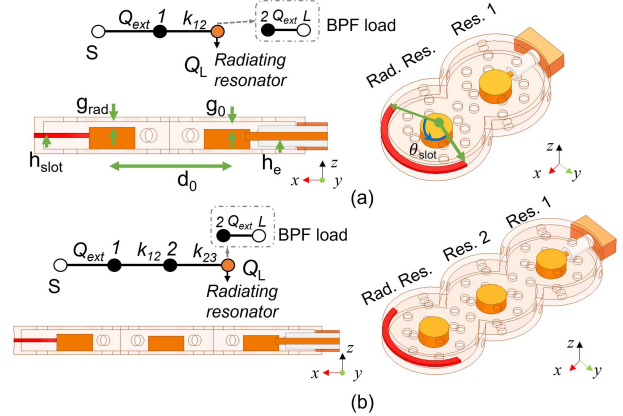
$$Q_L = (1 + k) \frac{f_0}{f_2 - f_1}, \quad k = \frac{1 - S_{11}^{\min}}{1 + S_{11}^{\min}}, \quad S_{11}^{\Phi} = \sqrt{\frac{1 + |S_{11}^{\min}|^2}{2}} \quad (2)$$

where k is the coupling coefficient between the SMA connector and the under-coupled resonator. $|S_{11}^{\min}|$ is the minimum $|S_{11}|$ at the f_0 . f_1 and f_2 are frequencies where $|S_{11}| = |S_{11}^{\min}|$, as shown in Fig. 5(b). Using full-wave EM simulations, Q_L and the operating frequency f_0 is extracted for different values of r_{slot} and g as depicted in Fig. 6(a) for the case of the top-slot antenna. Similarly, Q_L and f_0 for different values of θ_{slot} and g for the side-slot configuration is shown in Fig. 6(b). As it can be seen, Q_L and f_0 are altered by both the size of the slot and g . The Q_{ext} for different tapping locations of the SMA connector h_e is shown in Fig. 6(c).

For demonstration purposes, a first-order top-slot filtenna with fractional bandwidth (FBW) of 8%, center frequency f_0 of 4.8 GHz and maximum gain of 5.2 dBi is designed with $Q_{ext} = 18.8$ and $Q_L = 17.1$ and using (1), (2). For the desired response, an annular slot with $r_{slot} = 14$ mm, $\theta_{slot} = 180^\circ$, and tapping location $h_e = 3$ mm needs to be selected. The simulated realized gain and $|S_{11}|$ are plotted in Fig. 4(c).

C. Higher Order Filtenna Design

To demonstrate scalability of the concept to higher order gain functions, a second-order top-slot BPF response is designed with: FBW of 8%, $f_0 = 4.8$ GHz and maximum realized gain of


 Fig. 7. Second-order coaxial-resonator-based filtenna with a slot placed on the top. (a) CRD. (b) Side view. (c) Three-dimensional model. $a = 5$, $b = 15$, $d = 22.5$, $g_{rad} = 0.75$, $g_0 = 1.5$, $h_e = 3$, all units are in mm.

 Fig. 8. Second- and third-order coaxial-resonator-based filtennas with a slot placed on the side. (a) CRD and geometry details of the second-order filtenna. (b) CRD and geometry details of the third-order filtenna. $a = 5$, $b = 15$, $d = 24$, $g_{rad} = 1$, $g_0 = 1.4$, $h_e = 3$, $h_{slot} = 3$, all units are in mm.

5.2 dBi. To realize this gain function, Q_{ext} and Q_L in Fig. 7(a) are calculated using (1) ($Q_{ext} = 18.8$, $Q_L = 17.1$) and the inter-resonator coupling is calculated as $k_{12} = m_{12} \text{FBW} = 0.06$. The normalized coupling coefficients are $m_{01} = 0.85$ and $m_{12} = 0.75$. Having specified the desired coupling element values, the geometric parameters $r_{slot} = 14$ mm, $\theta_{slot} = 180^\circ$, and $h_e = 3$ mm are specified using the design curves in Fig. 6(a)–(c). Next, the distance d between of the two resonators is specified so that the desired k_{12} in the CRD in Fig. 5(a) is obtained using the design process in [24]. The relationship of k_{12} as a function of d is provided in Fig. 6(d), which indicates that a d equal to 24 mm needs to be selected.

Following the aforementioned design method, a second-order and a third-order side-slot filtennas can be designed, as shown in Fig. 8(a) and (b). In the case of the third-order filtenna, the coupling coefficients are $k_{12} = k_{23} = 0.064$, $Q_{ext} = 16.1$ for $\text{FBW} = 8\%$ and $f_0 = 4.6$ GHz, The normalized coupling coefficients are $m_{01} = 0.88$ and $m_{12} = m_{23} = 0.80$.

To facilitate monolithic integration using SLA-based manufacturing, nonradiating holes need to be opened on the outer walls of the filtenna so that the Cu-plating solution can flow into the cavity and allow for the internal walls to be metalized. Their size needs to be carefully selected so that they do not affect the Q_U of the coaxial resonators [24]. Fig. 9 depicts the surface H-field distribution of the second-order top-slot filtenna at 4.8 GHz. As it can be seen, it remains the same after adding the nonradiating holes, which indicates that those holes do not affect its EM performance.

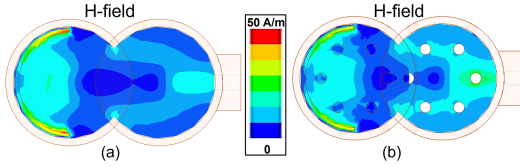


Fig. 9. H-field distribution on the surface of the upper wall of the second-order top-slot filtenna at 4.8 GHz. (a) Without holes. (b) With nonradiating holes.

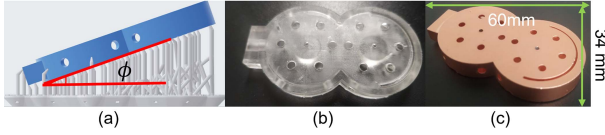


Fig. 10. Manufactured prototype of the second-order top-slot coaxial-resonator-based filtenna. (a) CAD model for SLA-based monolithic manufacturing. (b) Manufactured prototype before Cu-plating. (c) Manufactured prototype after Cu-plating.

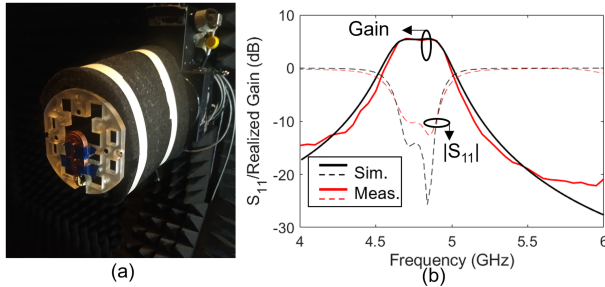


Fig. 11. (a) Measurement setup for the top-slot filtenna. (b) RF-measured and EM-simulated $|S_{11}|$ and realized gain of the second-order filtenna in Fig. 10.



Fig. 12. Manufactured prototypes of the side-slot coaxial-resonator-based filtenna before and after Cu-plating. (a) Second order. (b) Third order.

III. EXPERIMENTAL VALIDATION

For proof-of-concept validation purposes, a second-order top-slot filtenna, a second-order and a third-order side-slot filtenna with f_0 of 4.8, 4.65, and 4.65 GHz, and an FBW of 8% were prototyped using SLA 3-D printing. For monolithic integration, the filtenna model (Fig. 10) needs to be appropriately oriented with an angle of 30° within the DAM system and support structures need to be carefully added so that the model is fully supported and the supports can be readily removed after manufacturing. A commercially available Cu-plating process was employed that creates a Cu thickness of $50 \mu\text{m}$, which is $20\times$ larger than the skin depth at the designed frequency.

Fig. 10 depicts the CAD model for the SLA manufactured second-order top-slot filtenna before and after Cu-plating. The RF measured and EM simulated $|S_{11}|$ and maximum gain are depicted in Fig. 11 and are in fair agreement. The measured filtenna characteristics are summarized as follows: $f_0 = 4.75$ GHz, 3 dB FBW = 7.42%, maximum realized gain of 5.5 dBi, at 4.8 GHz. The manufactured second-order and third-order side-slot filtennas and their measured responses are shown in Figs. 12 and 13 and exhibit the following characteristics: second-order $f_0 = 4.85$ GHz, 3 dB FBW = 8.33%, maximum realized gain of 2.6 dBi; third-order $f_0 = 4.6$ GHz, 3 dB FBW = 7.61%,

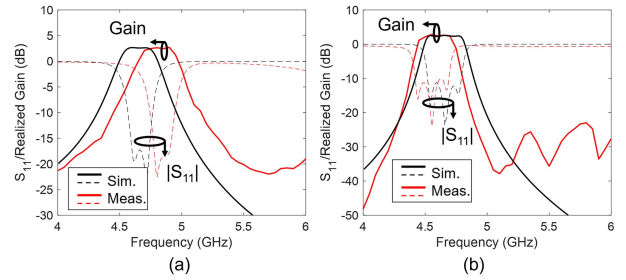


Fig. 13. Measured and EM-simulated $|S_{11}|$ and the maximum realized gain of the side-slot coaxial-resonator-based filtenna. (a) Second-order prototype [see Fig. 12(a)]. (b) Third-order prototype [see Fig. 12(b)].

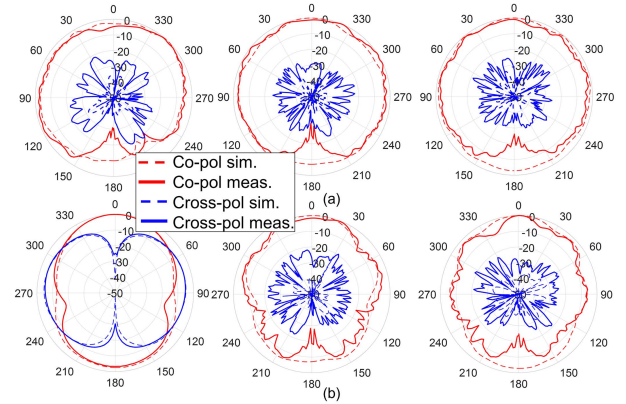


Fig. 14. Normalized co- and cross-pol of the coaxial-resonator-based filtenna. (a) E-plane (xz). (b) H-plane (zy for top-slot, xy for side-slot). From left to right, second-order top slot, second-order side slot, and third-order side slot.

TABLE I
COMPARISON WITH STATE-OF-THE-ART 3-D FILTENNAS

Ref.	Tech.	f_c (GHz)	#N	Gain	FBW(%)
[4]	SIW	9.8	4	6.1	6.0
[5]	SIW	10.2	2	4.9	3.0
[6]	Metal	3.5-3.7	2	6.5	5.8
[23]	SIW	2.3-2.6	1	5.5	N/A
T.W.(2P/S)	AM	4.85	2	2.6	8.33
T.W.(3P/S)	AM	4.6	3	2.6	7.61
T.W.(2P/T)	AM	4.75	2	5.5	7.42

(2P/S(T)): 2-pole side (top) slot, #N: number of poles, MS: microstrip, N/A: un-reported).

maximum realized gain of 2.6 dBi. The frequency shift is due to the fabrication tolerances. The measured normalized radiation patterns in the E- and H-planes at f_0 are provided in Fig. 14. Table I provides a comparison of the proposed coaxial resonator-based filtenna with other state-of-the-art 3-D filtennas using SIW and CNC manufacturing. As it can be seen, the proposed concept is the only one using 3-D coaxial cavity resonators and the very first one that is fabricated monolithically through SLA. Overall, a fair agreement has been achieved between the simulation and measurement, successfully validating the filtenna concept.

IV. CONCLUSION

The design, manufacturing, and measurement of a new class of highly miniaturized coaxial cavity-resonator-based filtennas is reported. Size compactness is achieved through the: 1) RF co-design of two RF components, 2) use of capacitively loaded coaxial resonators, and 3) monolithic integration enabled by SLA process. A second-order top-slot, a second-order and a third-order side-slot filtenna prototypes were manufactured and tested, exhibiting a fair agreement with EM simulations.

REFERENCES

- [1] Z. B. Khan and Z. Huiling, "Design of an equal division single band filtering power divider based on ring resonator band-pass filter," in *Proc. 11th Eur. Conf. Antennas Propag.*, Mar. 2017, pp. 1224–1227.
- [2] A. Ashley and D. Psychogiou, "RF co-designed bandpass filter/circulator with tunable center frequency, bandwidth, and out-of-band isolation," *IEEE Microw. Wireless Compon. Lett.*, vol. 31, no. 7, pp. 845–848, Jul. 2021.
- [3] C.-K. Lin and S.-J. Chung, "A compact filtering microstrip antenna with quasi-elliptic broadside antenna gain response," *IEEE Antennas Wireless Propag. Lett.*, vol. 10, pp. 381–384, 2011.
- [4] Y. Yusuf and X. Gong, "Compact low-loss integration of high-Q 3-D filters with highly efficient antennas," *IEEE Trans. Microw. Theory Techn.*, vol. 59, no. 4, pp. 857–865, Apr. 2011.
- [5] Y. Yusuf, H. Cheng, and X. Gong, "A seamless integration of 3-D vertical filters with highly efficient slot antennas," *IEEE Trans. Antennas Propag.*, vol. 59, no. 11, pp. 4016–4022, Nov. 2011.
- [6] R.-S. Chen et al., "Novel reconfigurable full-metal cavity-backed slot antennas using movable metal posts," *IEEE Trans. Antennas Propag.*, vol. 69, no. 10, pp. 6154–6164, Oct. 2021.
- [7] C. Pfeiffer, J. Massman, and T. Steffen, "3-D printed metallic dual-polarized vivaldi arrays on square and triangular lattices," *IEEE Trans. Antennas Propag.*, vol. 69, no. 12, pp. 8325–8334, Dec. 2021.
- [8] C. Stoumpos, J.-P. Frayssse, G. Goussetis, R. Sauleau, and H. Legay, "Quad-furcated profiled horn: The next generation highly efficient geo antenna in additive manufacturing," *IEEE Open J. Antennas Propag.*, vol. 3, pp. 69–82, 2022.
- [9] M. Ferrando-Rocher, J. I. Herranz-Herruzo, A. Valero-Nogueira, and B. Bernardo-Clemente, "Selective laser sintering manufacturing as a low cost alternative for flat-panel antennas in millimeter-wave bands," *IEEE Access*, vol. 9, pp. 45721–45729, 2021.
- [10] S. Wang et al., "3-D printed zirconia ceramic Archimedean spiral antenna: Theory and performance in comparison with its metal counterpart," *IEEE Antennas Wireless Propag. Lett.*, vol. 21, no. 6, pp. 1173–1177, Jun. 2022.
- [11] I. Goode and C. E. Saavedra, "3D printed linearly polarized X-band conical horn antenna and lens," *IEEE Open J. Antennas Propag.*, vol. 3, pp. 549–556, 2022.
- [12] Z. Y. Lopez, Z. Akhter, and A. Shamim, "3D printed RFID tag antenna miniaturized through volumetric folding and slow-wave structures," *IEEE J. Radio Freq. Identification*, vol. 6, pp. 164–175, 2022.
- [13] M. Kacar, T. M. Weller, and G. Mumcu, "3D printed wideband multilayered dual-polarized stacked patch antenna with integrated MMIC switch," *IEEE Open J. Antennas Propag.*, vol. 2, pp. 38–48, 2021.
- [14] Y.-X. Sun, D. Wu, and J. Ren, "Millimeter-wave dual-polarized dielectric resonator reflectarray fabricated by 3D printing with high relative permittivity material," *IEEE Access*, vol. 9, pp. 103795–103803, 2021.
- [15] M. Cuevas, F. Pizarro, A. Leiva, G. Hermosilla, and D. Yunge, "Parametric study of a fully 3D-printed dielectric resonator antenna loaded with a metallic cap," *IEEE Access*, vol. 9, pp. 73771–73779, 2021.
- [16] C. Pontì, P. Baccarelli, S. Ceccuzzi, and G. Schettini, "Tapered all-dielectric EBGs with 3-D additive manufacturing for high-gain resonant-cavity antennas," *IEEE Trans. Antennas Propag.*, vol. 69, no. 5, pp. 2473–2480, May 2021.
- [17] A. Molaei et al., "3-D-printed E-band compressive horn antenna for high-sensing-capacity imaging applications," *IEEE Antennas Wireless Propag. Lett.*, vol. 17, no. 9, pp. 1639–1642, Sep. 2018.
- [18] S. Sarjoghian, Y. Alfadhli, X. Chen, and C. G. Parini, "A 3-D-printed high-dielectric materials-filled pyramidal double-ridged horn antenna for abdominal fat measurement system," *IEEE Trans. Antennas Propag.*, vol. 69, no. 1, pp. 64–73, Jan. 2021.
- [19] R. Dubrovka, A. S. Andy, E. Saleh, R. C. Jones, R. S. Donnan, and C. J. Tuck, "Additive manufacturing of a terahertz back-to-back horn antenna for use in life sciences," *IEEE Trans. Compon., Packag., Manuf. Technol.*, vol. 12, no. 4, pp. 595–601, Apr. 2022.
- [20] K. Lomakin, S. Alhasson, and G. Gold, "Additively manufactured amplitude tapered slotted waveguide array antenna with horn aperture for 77 GHz," *IEEE Access*, vol. 10, pp. 44271–44277, 2022.
- [21] G. P. Le Sage, "3D printed waveguide slot array antennas," *IEEE Access*, vol. 4, pp. 1258–1265, 2016.
- [22] G. L. Matthaei, "Comb-line band-pass filters of narrow or moderate bandwidth," *Microw. J.*, vol. 6, pp. 82–91, Aug. 1963.
- [23] A. Semnani, M. D. Sinanis, and D. Peroulis, "An evanescent-mode cavity-backed high-power tunable slot antenna," *IEEE Trans. Antennas Propag.*, vol. 67, no. 6, pp. 3712–3719, Jun. 2019.
- [24] K. Zhao and D. Psychogiou, "Monolithic SLA-based capacitively-loaded high-Q coaxial resonators and bandpass filters," in *Proc. 49th Eur. Microw. Conf.*, Jan. 2021, pp. 471–474.